

REPORT DOCUMENTATION PAGE				<i>Form Approved</i> OMB No. 0704-0188	
Public reporting burden for this collection of information is estimated to average 1 hour per response, including the time for reviewing instructions, searching existing data sources, gathering and maintaining the data needed, and completing and reviewing this collection of information. Send comments regarding this burden estimate or any other aspect of this collection of information, including suggestions for reducing this burden to Department of Defense, Washington Headquarters Services, Directorate for Information Operations and Reports (0704-0188), 1215 Jefferson Davis Highway, Suite 1204, Arlington, VA 22202-4302. Respondents should be aware that notwithstanding any other provision of law, no person shall be subject to any penalty for failing to comply with a collection of information if it does not display a currently valid OMB control number. PLEASE DO NOT RETURN YOUR FORM TO THE ABOVE ADDRESS.					
1. REPORT DATE (DD-MM-YYYY) 01-12-2010		2. REPORT TYPE Article		3. DATES COVERED (From - To) DEC 2010 - JAN 2011	
4. TITLE AND SUBTITLE A Technique for Real-Time Shadowing Adjustment of RCS Scattering Center Models				5a. CONTRACT NUMBER FA8720-05-C-0002	
				5b. GRANT NUMBER	
				5c. PROGRAM ELEMENT NUMBER	
6. AUTHOR(S) Joshua L. Wilson, Brian W. Rybicki, Lea E. Johnson, and Douglas M. Koltenuk				5d. PROJECT NUMBER	
				5e. TASK NUMBER	
				5f. WORK UNIT NUMBER	
7. PERFORMING ORGANIZATION NAME(S) AND ADDRESS(ES) MIT Lincoln Laboratory 244 Wood Street Lexington, MA 02420				8. PERFORMING ORGANIZATION REPORT NUMBER	
9. SPONSORING / MONITORING AGENCY NAME(S) AND ADDRESS(ES) PEO IWS 2RAX				10. SPONSOR/MONITOR'S ACRONYM(S) NAVY	
				11. SPONSOR/MONITOR'S REPORT NUMBER(S)	
12. DISTRIBUTION / AVAILABILITY STATEMENT DISTRIBUTION STATEMENT A. Approved for public release; distribution is unlimited.					
13. SUPPLEMENTARY NOTES					
14. ABSTRACT A method has been developed to adjust Radar Cross Section (RCS) scattering models for two-body effects, particularly shadowing. The method described here involves using the near field scattering solution of one object to apply two-body corrections to another. By assuming that the second object can be represented by a known set of point scatterers, the fields at these scattering centers are used to calculate the adjusted RCS in the presence of the shadowing object using the principle of reciprocity. Since this approximation does not require a full-wave electromagnetic solution, it is considerably more computationally efficient than Moment Method solvers or other similar techniques, and thus could be adapted to real-time applications. The results of the method are compared against measurement and Moment Method simulation for the case of two cylinders, a cylinder and a cone, and two spheres. Good agreement is generally obtained between the proposed approximate model and measurements or Moment Method simulations.					
15. SUBJECT TERMS Electromagnetic scattering, Radar cross sections, Numerical techniques.					
16. SECURITY CLASSIFICATION OF: U			17. LIMITATION OF ABSTRACT SAR	18. NUMBER OF PAGES 10	19a. NAME OF RESPONSIBLE PERSON Zach Sweet
a. REPORT U	b. ABSTRACT U	c. THIS PAGE U			19b. TELEPHONE NUMBER (include area code) 781-981-5997

A Technique for Real-Time Shadowing Adjustment of RCS Scattering Center Models

Joshua L. Wilson, Brian W. Rybicki, Lea E. Johnson, and Douglas M. Koltenuk

Abstract—A method has been developed to adjust Radar Cross Section (RCS) scattering models for two-body effects, particularly shadowing. The method described here involves using the near field scattering solution of one object to apply two-body corrections to another. By assuming that the second object can be represented by a known set of point scatterers, the fields at these scattering centers are used to calculate the adjusted RCS in the presence of the shadowing object using the principle of reciprocity. Since this approximation does not require a full-wave electromagnetic solution, it is considerably more computationally efficient than Moment Method solvers or other similar techniques, and thus could be adapted to real-time applications.

The results of the method are compared against measurement and Moment Method simulation for the case of two cylinders, a cylinder and a cone, and two spheres. Good agreement is generally obtained between the proposed approximate model and measurements or Moment Method simulations.

Index Terms—Electromagnetic scattering, Radar cross sections, Numerical techniques.

I. INTRODUCTION

RADAR scattering involving multiple bodies can often be treated by superposing the returns from each of the individual scatterers in the scene. However, the situation becomes more complicated when either the geometry of the objects or their proximity to one another demands that two-body electromagnetic interactions be taken into account. A number of radar scenes, such as those encountered in space sensing, exhibit two-body phenomena. Modeling and understanding these interactions are necessary to construct an accurate model of the entire scattering scene.

It has been shown [1] that the reaction theorem can be applied iteratively to find two-body scattering corrections, and that even a first-order approximation can yield good results in many cases. This approach simplifies the computation significantly from what would be required if a full-wave simulation were performed with both objects present. A similar approach was used by Li *et al.* in [2]. However, the technique involves integration of the field quantities across the surface of the object. In this paper, we work with a scattering center representation of the object, and these scattering centers are adjusted to account for two-body interactions. We will see that the technique can be applied to shadowing objects of any geometry provided that reasonable analytic expressions can be found for the near-field scattering solution of one of the objects (e.g., a conducting plate, cylinder, sphere, etc.).

In this paper, we will first show how the known fields from a single object can be used to adjust a scattering center model to

account for two-body interactions. Then, we will present three examples of one object shadowing another for both TE and TM polarizations, one case for two finite cylinders, one for a cylinder and a cone, and finally a case for two spheres. We will show numerical results compared to static range measurements as well as simulations carried out in CICERO, a Moment Method-based solver.

II. TECHNIQUE FOR SCATTERING CENTER ADJUSTMENT

A. Power Adjustment

We assume that the shadowed body can be decomposed into discrete scattering centers, each of which can be shadowed independently based on its physical location in space. For a scattering center at a fixed location \mathbf{r} , the radar equation gives

$$P_R = \frac{P_T G_T}{4\pi r^2} \sigma \frac{1}{4\pi r^2} \frac{G_R \lambda^2}{4\pi}. \quad (1)$$

Recognizing $\frac{P_T G_T}{4\pi r^2}$ as the magnitude of the incident radiation intensity at the scatterer of interest $\mathbf{S}_i(\mathbf{r})$, and $P_R \frac{4\pi}{G_R \lambda^2}$ as the magnitude of the intensity at the receiver \mathbf{S}_r , we have

$$|\mathbf{S}_r| = |\mathbf{S}_i(\mathbf{r})| \sigma \frac{1}{4\pi r^2}. \quad (2)$$

We now associate the intensity vector \mathbf{S} with the square of the value of the magnetic field \mathbf{H} , and write

$$H_r = H_i(\mathbf{r}) \sqrt{\sigma} \frac{1}{2r\sqrt{\pi}}. \quad (3)$$

If we now consider the behavior of the scatterer in the presence of the shadowing object, we first recognize that the incident radiation at the scattering center at \mathbf{r} is no longer $H_i(\mathbf{r})$, but rather

$$H'_i(\mathbf{r}) = G_1 H_i(\mathbf{r}) \quad (4)$$

for some $G_1(\mathbf{r})$. So, $H'_i(\mathbf{r})$ is the field at \mathbf{r} due to an incident field $H_i(\mathbf{r})$ in the presence of the shadowing object. H_r must also be adjusted, since the power has to be reradiated from the scatterer in the presence of the shadowing object, so another correction must be made to (3):

$$H'_r = H'_i(\mathbf{r}) \sqrt{\sigma} G_2 \frac{1}{2r\sqrt{\pi}}, \quad (5)$$

for some $G_2(\mathbf{r})$. So finally we have

$$H'_r = G_1 H_i(\mathbf{r}) \sqrt{\sigma} G_2 \frac{1}{2r\sqrt{\pi}}. \quad (6)$$

By reciprocity,

$$G_1 = G_2 \quad (7)$$

so

$$H'_r = (G_1)^2 H_i(\mathbf{r}) \sqrt{\sigma} \frac{1}{2r\sqrt{\pi}}, \quad (8)$$

and the adjusted RCS value is

$$\sqrt{\sigma'} = (G_1)^2 \sqrt{\sigma}. \quad (9)$$

This simplified case uses scalar power quantities rather than the actual field vector components; however, this provides a simple pedagogical starting point which will make the vector analysis in the next section more clear.

B. Adjustment of Field Quantities

We must now elaborate on the treatment of the scattering center adjustment in order to account for both the phase and polarization of the shadowed return. These quantities proceed from the time-varying three-dimensional nature of the fields and are not calculable from the analysis of the previous section.

We consider as a source a single magnetic dipole located far away from the target complex, such that the field at the target can be approximated as a plane wave whose magnetic field vector is parallel to the direction of the dipole. Thus, it is possible to construct a dyadic Green's function in the presence of a shadowing cylinder at any location \mathbf{r}_2 , such that

$$\mathbf{H}(\mathbf{r}_2) = \iiint_V \mathbf{M}(\mathbf{r}') \cdot \bar{\mathbf{G}}(\mathbf{r}_2, \mathbf{r}') dv', \quad (10)$$

which reduces, assuming an impulse source at \mathbf{r}_1 , to

$$\mathbf{H}(\mathbf{r}_2) = \mathbf{M}(\mathbf{r}_1) \cdot \bar{\mathbf{G}}(\mathbf{r}_2, \mathbf{r}_1). \quad (11)$$

We will assume a simple object shape so that this Green's function can be computed fairly easily. One could also use the Green's function for the electric field and electric sources, though no comparisons have been made thus far between these two approaches.

The scatterer at \mathbf{r}_2 will then radiate a scattered field in response to the impinging field. We can assume that this field is due to a particular impulse magnetic current \mathbf{M}_2 . Thus, associating \mathbf{M}_1 and \mathbf{H}_1 with the incident fields, and \mathbf{M}_2 and \mathbf{H}_2 with the scattered fields, we have by reciprocity

$$\mathbf{M}_1(\mathbf{r}_1) \cdot \mathbf{H}_2(\mathbf{r}_1) = \mathbf{M}_2(\mathbf{r}_2) \cdot \mathbf{H}_1(\mathbf{r}_2). \quad (12)$$

Substituting the appropriate expressions for \mathbf{H}_1 and \mathbf{H}_2 as in (11),

$$\begin{aligned} & \mathbf{M}_1(\mathbf{r}_1) \cdot (\mathbf{M}_2(\mathbf{r}_2) \cdot \bar{\mathbf{G}}(\mathbf{r}_1, \mathbf{r}_2)) \\ &= \mathbf{M}_2(\mathbf{r}_2) \cdot (\mathbf{M}_1(\mathbf{r}_1) \cdot \bar{\mathbf{G}}(\mathbf{r}_2, \mathbf{r}_1)) \\ &= (\mathbf{M}_1(\mathbf{r}_1) \cdot \bar{\mathbf{G}}(\mathbf{r}_2, \mathbf{r}_1)) \cdot \mathbf{M}_2(\mathbf{r}_2) \end{aligned} \quad (13)$$

from which we conclude that

$$\bar{\mathbf{G}}(\mathbf{r}_1, \mathbf{r}_2) = \bar{\mathbf{G}}(\mathbf{r}_2, \mathbf{r}_1)^T. \quad (14)$$

To complete our formulation of the problem, we must relate $\mathbf{M}_2(\mathbf{r}_2)$ to $\mathbf{H}_1(\mathbf{r}_2)$, i.e., how the scatterer responds to an incident field. We will express the magnetic current at the scattering center location as an impulse magnetic current. It

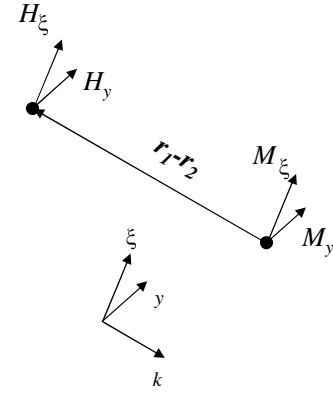


Fig. 1. Definition of (k, y, ξ) coordinate system.

is well known that a \hat{z} directed magnetic dipole located at the origin of magnitude M_0 produces a field

$$H_\theta = \frac{j\beta M_0}{\eta_0 4\pi r} e^{-j\beta r} \sin \theta. \quad (15)$$

We will use two such magnetic currents directed in orthogonal directions and require that the field emitted from this crossed dipole pair be equivalent to the scattered field required by the RCS of the particular scatterer in question. To do this, we first express the fields in terms of basis vectors \hat{k} , \hat{y} and $\hat{\xi}$, defined as in Fig. 1 such that $\hat{\xi}$ is in the xz plane and

$$\hat{k} \times \hat{y} = \hat{\xi}. \quad (16)$$

In this convention, the incident magnetic field is directed along \hat{y} for the TM or “H” polarization case and along $\hat{\xi}$ for the TE or “V” polarization case (wave propagation is along \hat{k}). We will neglect all sources and fields directed along \hat{k} , since these will disappear in the far field. Since the vector $\mathbf{r}_1 - \mathbf{r}_2$ is parallel to \hat{k} , we can neglect the $\sin \theta$ terms, leaving

$$H_y(\mathbf{r}_1) = \frac{j\beta M_{2y}}{\eta_0 4\pi |\mathbf{r}_1 - \mathbf{r}_2|} e^{-j\beta |\mathbf{r}_1 - \mathbf{r}_2|}, \quad (17)$$

$$H_\xi(\mathbf{r}_1) = \frac{j\beta M_{2\xi}}{\eta_0 4\pi |\mathbf{r}_1 - \mathbf{r}_2|} e^{-j\beta |\mathbf{r}_1 - \mathbf{r}_2|},$$

where \mathbf{M}_2 specifies the impulse source at the scattering center at \mathbf{r}_2 . Therefore,

$$M_{2y} = \frac{-j4\pi |\mathbf{r}_1 - \mathbf{r}_2| \eta_0 H_y(\mathbf{r}_1)}{\beta} e^{j\beta |\mathbf{r}_1 - \mathbf{r}_2|}, \quad (18)$$

$$M_{2\xi} = \frac{-j4\pi |\mathbf{r}_1 - \mathbf{r}_2| \eta_0 H_\xi(\mathbf{r}_1)}{\beta} e^{j\beta |\mathbf{r}_1 - \mathbf{r}_2|}.$$

$H_y(\mathbf{r}_1)$ and $H_\xi(\mathbf{r}_1)$ can then be related to the field impinging on the scatterer by invoking the known scatterer RCS:

$$\bar{\sigma} = \begin{pmatrix} 0 & 0 & 0 \\ 0 & HH & HV \\ 0 & VH & VV \end{pmatrix}, \quad (19)$$

where the components of the matrix in the $ky\xi$ basis involve the horizontal and vertical components of the scattering matrix. From the definition of RCS in terms of magnetic field quantities, one can write

$$\mathbf{H}(\mathbf{r}_1) = \frac{1}{2|\mathbf{r}_1 - \mathbf{r}_2|\sqrt{\pi}} \mathbf{H}_1(\mathbf{r}_2) \cdot \sqrt{\sigma}, \quad (20)$$

assuming that the distance $\mathbf{r}_1 - \mathbf{r}_2$ is sufficiently large. Note that the field $\mathbf{H}(\mathbf{r}_1)$ here is the field due to the scattering center in the absence of a shadowing body. Substituting this into (18),

$$\mathbf{M}_2(\mathbf{r}_2) = A \left(\mathbf{H}_1(\mathbf{r}_2) \cdot \sqrt{\sigma} \right), \quad (21)$$

where

$$A = \frac{-2j\sqrt{\pi}\eta_0 e^{j\beta|\mathbf{r}_1 - \mathbf{r}_2|}}{\beta}. \quad (22)$$

Then,

$$\begin{aligned} \mathbf{H}_2(\mathbf{r}_1) &= \mathbf{M}_2(\mathbf{r}_2) \cdot \bar{\mathbf{G}}(\mathbf{r}_1, \mathbf{r}_2) \\ &= \left(A \mathbf{H}_1(\mathbf{r}_2) \cdot \sqrt{\sigma} \right) \cdot \bar{\mathbf{G}}(\mathbf{r}_1, \mathbf{r}_2) \\ &= \left(A \left(\mathbf{M}_1(\mathbf{r}_1) \cdot \bar{\mathbf{G}}(\mathbf{r}_2, \mathbf{r}_1) \right) \cdot \sqrt{\sigma} \right) \cdot \bar{\mathbf{G}}(\mathbf{r}_1, \mathbf{r}_2) \\ &= A \mathbf{M}_1(\mathbf{r}_1) \cdot \left(\bar{\mathbf{G}}(\mathbf{r}_2, \mathbf{r}_1) \cdot \sqrt{\sigma} \cdot \bar{\mathbf{G}}(\mathbf{r}_1, \mathbf{r}_2) \right) \\ &= A \mathbf{M}_1(\mathbf{r}_1) \cdot \left(\bar{\mathbf{G}}(\mathbf{r}_2, \mathbf{r}_1) \cdot \sqrt{\sigma} \cdot \bar{\mathbf{G}}(\mathbf{r}_2, \mathbf{r}_1)^T \right). \end{aligned} \quad (23)$$

From

$$\mathbf{M}_1(\mathbf{r}_1) = \frac{-j4\pi|\mathbf{r}_1 - \mathbf{r}_2|\eta_0 \mathbf{H}_i(\mathbf{r}_2) e^{j\beta|\mathbf{r}_1 - \mathbf{r}_2|}}{\beta}, \quad (24)$$

where $\mathbf{H}_i(\mathbf{r}_2)$ is the incident field in the absence of the shadowing body,

$$\begin{aligned} \mathbf{H}_2(\mathbf{r}_1) &= A \frac{-j4\pi|\mathbf{r}_1 - \mathbf{r}_2|\eta_0 e^{j\beta|\mathbf{r}_1 - \mathbf{r}_2|}}{\beta} \mathbf{H}_i(\mathbf{r}_2) \cdot \\ &\quad \left(\bar{\mathbf{G}}(\mathbf{r}_2, \mathbf{r}_1) \cdot \sqrt{\sigma} \cdot \bar{\mathbf{G}}(\mathbf{r}_2, \mathbf{r}_1)^T \right) \\ &= \frac{-8\pi^{\frac{3}{2}}|\mathbf{r}_1 - \mathbf{r}_2|\eta_0^2 e^{2j\beta|\mathbf{r}_1 - \mathbf{r}_2|}}{\beta^2} \mathbf{H}_i(\mathbf{r}_2) \cdot \\ &\quad \left(\bar{\mathbf{G}}(\mathbf{r}_2, \mathbf{r}_1) \cdot \sqrt{\sigma} \cdot \bar{\mathbf{G}}(\mathbf{r}_2, \mathbf{r}_1)^T \right). \end{aligned} \quad (25)$$

Finally, comparing this relation with the formula defining the adjusted RCS value

$$\mathbf{H}_2(\mathbf{r}_1) = \frac{1}{2\sqrt{\pi}|\mathbf{r}_1 - \mathbf{r}_2|} \mathbf{H}_i(\mathbf{r}_2) \cdot \sqrt{\sigma_{new}}, \quad (26)$$

we conclude

$$\begin{aligned} \sqrt{\sigma_{new}} &= \frac{-16\pi^2|\mathbf{r}_1 - \mathbf{r}_2|^2\eta_0^2 e^{2j\beta|\mathbf{r}_1 - \mathbf{r}_2|}}{\beta^2} \times \\ &\quad \left(\bar{\mathbf{G}}(\mathbf{r}_2, \mathbf{r}_1) \cdot \sqrt{\sigma} \cdot \bar{\mathbf{G}}(\mathbf{r}_2, \mathbf{r}_1)^T \right). \end{aligned} \quad (27)$$

We can simplify this expression to

$$\sqrt{\sigma_{new}} = \bar{\mathbf{G}}'(\mathbf{r}_2, \mathbf{r}_1) \cdot \sqrt{\sigma} \cdot \bar{\mathbf{G}}'(\mathbf{r}_2, \mathbf{r}_1)^T, \quad (28)$$

where $\bar{\mathbf{G}}'$ is defined such that

$$\bar{\mathbf{G}} = \bar{\mathbf{G}}' \cdot \bar{\mathbf{G}}_0, \quad (29)$$

with $\bar{\mathbf{G}}_0$ being the free space Green's function. $\bar{\mathbf{G}}'$ represents the ratio of $\bar{\mathbf{G}}$ to the free space Green's function as well as the ratio of the magnetic field at \mathbf{r}_2 to an incident plane wave of unity amplitude.

The similarities with the scalar case considered in the last section are now apparent. Whereas before in (8), we had the incident and scattered fields related by a real scalar quantity $G\sqrt{\sigma}G$, we now have them related by a dyadic quantity

$\bar{\mathbf{G}}(\mathbf{r}_2, \mathbf{r}_1) \cdot \sqrt{\sigma} \cdot \bar{\mathbf{G}}(\mathbf{r}_2, \mathbf{r}_1)^T$. The validity of this technique hinges on how accurately the point scatterer approximation represents the true scattering behavior of the second object. It will be shown in the next section that reasonably accurate results are possible.

The method could be extended to more than one shadowing object. In this case, the Green's function in the presence of two or more objects would have to be calculated. If the shadowing objects are far apart and not both along the line-of-sight, calculation of the combined Green's function can generally be approximated by simply applying superposition to the scattered fields from each object in isolation.

As an example case, let us assume that the entire scattering scene has rotational symmetry, such as the case of two axially aligned cylinders considered in the next section. In the (k, y, ξ) coordinate system,

$$\begin{aligned} \bar{\mathbf{G}}(\mathbf{r}_2, \mathbf{r}_1) \cdot \sqrt{\sigma} \cdot \bar{\mathbf{G}}(\mathbf{r}_2, \mathbf{r}_1)^T &= \\ \begin{pmatrix} 0 & 0 & 0 \\ 0 & g_{yy} & g_{y\xi} \\ 0 & g_{\xi y} & g_{\xi\xi} \end{pmatrix} \cdot \sqrt{\sigma} \cdot \begin{pmatrix} 0 & 0 & 0 \\ 0 & g_{yy} & g_{\xi y} \\ 0 & g_{y\xi} & g_{\xi\xi} \end{pmatrix}. \end{aligned} \quad (30)$$

If we take the rotation axis of the body to be the z axis and the xz plane as the the plane of incidence, all scattering centers will lie in the xz plane, and at these observation points we can argue by symmetry that

$$\begin{aligned} g_{y\xi} &= 0 \\ g_{\xi y} &= 0. \end{aligned} \quad (31)$$

Likewise, it has been shown [3] that for a body of revolution, the VH and HV RCS polarization components will be zero for a monostatic measurement. Therefore, the corrected RCS for a body of revolution scatterer is

$$\bar{\mathbf{G}}(\mathbf{r}_2, \mathbf{r}_1) \cdot \sqrt{\sigma} \cdot \bar{\mathbf{G}}(\mathbf{r}_2, \mathbf{r}_1)^T = \begin{pmatrix} 0 & 0 & 0 \\ 0 & g_{yy}^2 HH & 0 \\ 0 & 0 & g_{\xi\xi}^2 VV \end{pmatrix}. \quad (32)$$

As expected, the scattering matrix is diagonalized when rotationally symmetric objects are considered. Moreover, the corrected VV component has no dependence on the original HH component, and vice versa. This also implies that for problems with rotational symmetry, only one field component has to be computed at the observation point for each incident polarization.

Some caution must be taken regarding the applicability of the model for predicting multi-bounce returns. In assuming that a scattering center is well-defined by its VV , HH , HV , and VH components at a particular aspect, we have assumed that the wave scattered by the shadower and the incident wave are aligned. If this is not the case (such as in some multi-bounce situations) the scattering center must be redefined based on its bistatic response for at least two incident angles. This problem becomes exponentially more difficult and puts unrealistic requirements on the input scattering center model. However, as we will see later, the present technique does apply fairly well to shadowing corrections. The technique should also work in cases where the scattering centers are nearly isotropic.

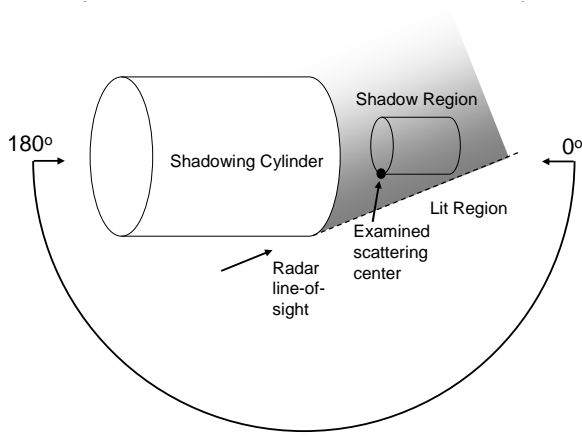


Fig. 2. Geometry of narrowband scenario defining aspect angle convention. The position of the cylinders is fixed and the aspect is varied.

III. RESULTS AND DISCUSSION

To validate the treatment of the two-body problem outlined in the previous section, comparisons are made with predicted results generated using first-principle codes as well as measurement results. This will be done through three example cases: the case of two cylinders, the case of a cylinder and a cone, and the case of two spheres.

A. Axially Aligned Cylinders

The validation scenario discussed in this section consists of two axially-aligned cylinders as shown in Fig. 2. The shadowing cylinder is 1.50 m in length and 0.15 m in radius. The shadowed cylinder is 0.30 m in length and 0.06 m in radius. The separation between the two cylinders is 0.15 m. The primary frequency used to probe the two-body scattering results is 8.5 GHz.

The scenario dimensions relative to a 0.035 m wavelength at 8.5 GHz require a near-field analysis of the shadowing cylinder as presented in the Appendix. Method of Moments (MoM) predictive codes can also be used to represent near-field scattering phenomenology. Due to the axial symmetry of these objects, the two-dimensional MoM solver CICERO (Code for Inhomogeneously Coated Electrically Reflecting Objects) can be used [4]. The scattering returns for the shadowed cylinder are first calculated without the shadowing object. These results can be used to determine scattering center strengths at various target locations as a function of aspect angle and polarization. The methods of Section II can be then used to determine the corrections to the strength of these scatterers due to the fields of the shadowing object described in the Appendix, and these corrections can be compared to the predicted results of the two-body system using CICERO.

A frequency band of 6.5 to 10.5 GHz is used with a 40 MHz frequency spacing to provide sufficient resolution for extracting scatterer intensity and to minimize interference between scatterers. The wideband scatterer strengths are extracted from Inverse Synthetic Aperture Radar (ISAR) images generated from the predicted complex RCS from CICERO with a six-degree window of aspect angles. The results are shown in Fig.

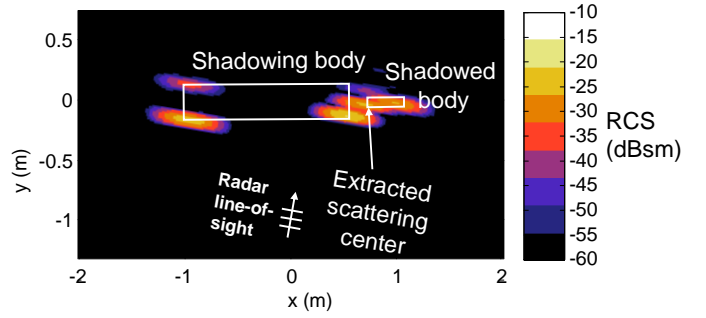


Fig. 3. Example image formed from CICERO two-body output, showing extracted scatterer (HH Polarization). Computed within a 6° window centered at 100.8° .

3. In this figure, the plane wave can be visualized as coming from the bottom-left of the picture, corresponding to a 100.8° incident angle.

From this wideband image, scatterers can be isolated from the shadowed target-only prediction, and changes to those scatterers can be observed when the shadowing object is added to the simulation. The extracted scatterer strengths are then compared with the estimations using the methods of Section II calculated at the center of the imaged band, 8.5 GHz.

There are a few caveats that must be taken into account for this analysis. The analysis of the fields of a finite cylinder (see the Appendix) assumed that the shadowing cylinder had no endcaps. CICERO requires that the modeled objects be closed, so the results of the two approaches differ as the aspect angle approaches the symmetry axis. Also, the endcaps produce significant scattering (including multi-bounce) at certain aspect angles in the CICERO prediction. To reduce this contribution, a dielectric absorbing layer has been added to the shadowing endcap.

1) *Narrowband Analysis:* The scatterer used for comparison purposes in this section is marked in Fig. 3. Aspect angle is defined with zero degrees pointing to the base of the shadowed cylinder. The two-body RCS corrections for HH and VV polarizations, extracted from a series of images similar to Fig. 3 have been plotted in Fig. 4. At low aspect angles, the shadowed object is in front of the shadowing object and is not shadowed. Beyond 90 degrees aspect, the scatterer RCS begins to oscillate due to edge diffraction from the shadowing cylinder. The diffracted ray begins to alternately interfere constructively and destructively with the line-of-sight contribution. Between 130 and 150 degrees the scatterer gradually begins to enter the shadow region as the direct path between the radar and the scatterer becomes blocked. Based on a geometric (ray-tracing) analysis, a sharp shadow boundary at 150 degrees would be observed by the shadowing cylinder. However, significant diffraction is observed, causing a blurring of the shadow boundary. Due to the lack of endcaps on the cylinder the scatterer RCS becomes strong again near 180 degrees. The predicted correction factors at 8.5 GHz are next added to the CICERO one-body extracted results and compared to the extracted two-body results. Fig. 5 (HH polarization) and 6 (VV polarization) show the CICERO

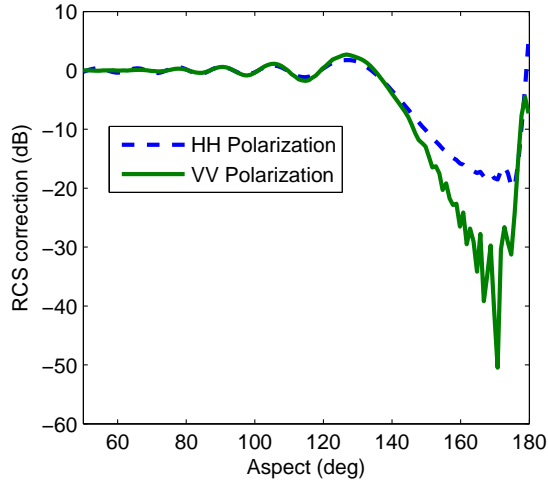


Fig. 4. Two-body corrections predicted by current method for HH and VV incident polarizations at 8.5 GHz.

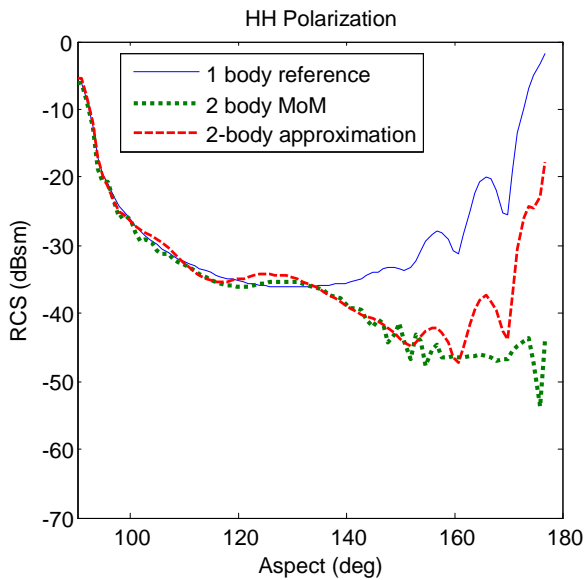


Fig. 5. Comparison of shadowing predictions for HH polarization.

one-body RCS extracted for the scatterer, the CICERO two-body scatterer RCS, and the CICERO one-body scatterer RCS adjusted by the present two-body model. The results of the two-body prediction and the corrected one-body scatterer RCS are in very good agreement in the critical region near the classical shadow boundary (from around 110 to 150 degrees), providing strong validation for the two-body model presented in this paper. Both CICERO and the two-body model indicate that the shadowing is greater for VV polarization than for HH polarization.

2) *Broadband Characteristics*: To study the correction factor behavior in wideband, these factors are calculated from 8-12 GHz for a scatterer near a cylinder centered at the origin with length 3.00 m and radius 0.50 m. The scatterer is placed 0.15 m away from the end of the cylinder ($z=1.65$ m), and its radial position (x) is moved from -1 m to 0.5 m at 1 m/s. This geometry is illustrated in Fig. 7. Fig. 8 shows a Range-

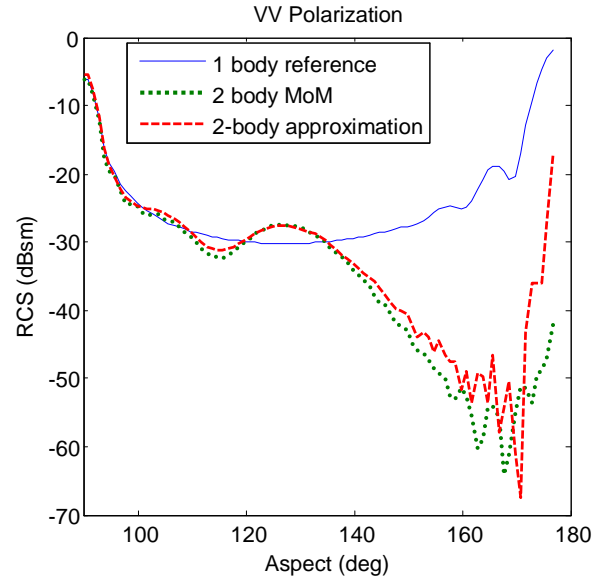


Fig. 6. Comparison of shadowing predictions for VV polarization.

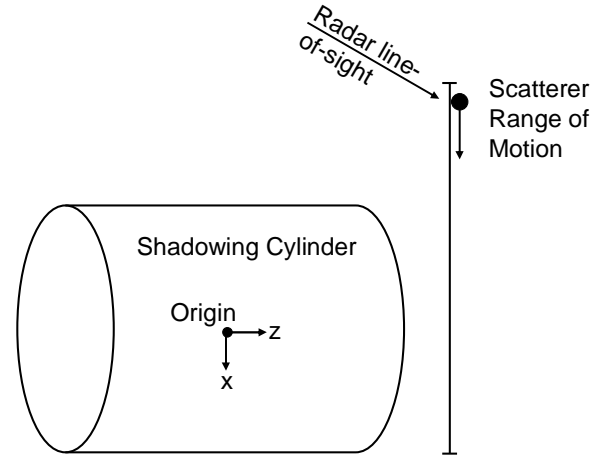


Fig. 7. Geometry of broadband scenario, showing scatterer at fixed axial position and varying radial position.

Time-Intensity (RTI) plot obtained by applying an FFT to the shadowing correction as calculated at a fixed 30 degree aspect angle over the entire bandwidth. Note that in this plot time can be equated to the radial position of the primary scatterer. Three distinct regions are observed in the RTI. Region 1 is characterized by two delayed scatterers in addition to the line-of-sight scatterer. These additional scatterers arise from the reflected ray paths from the shadowing cylinder to the physical point scatterer. The range to the middle scatterer (representing a bounce off the cylinder and a bounce off the scattering center) has constant RCS, whereas the downrange scatterer (representing two bounces off the cylinder and one off the scattering center) moves in-range as x increases. Some ripple is present as the three scatterers converge. This interference is a consequence of the finite bandwidth and is not related to shadowing. Region 2 is dominated by the incident wave, although some diffraction of the scattered wave from the cylinder edge is also observed. There is only minimal correction to the scatterer RCS in this region. In Region 3,

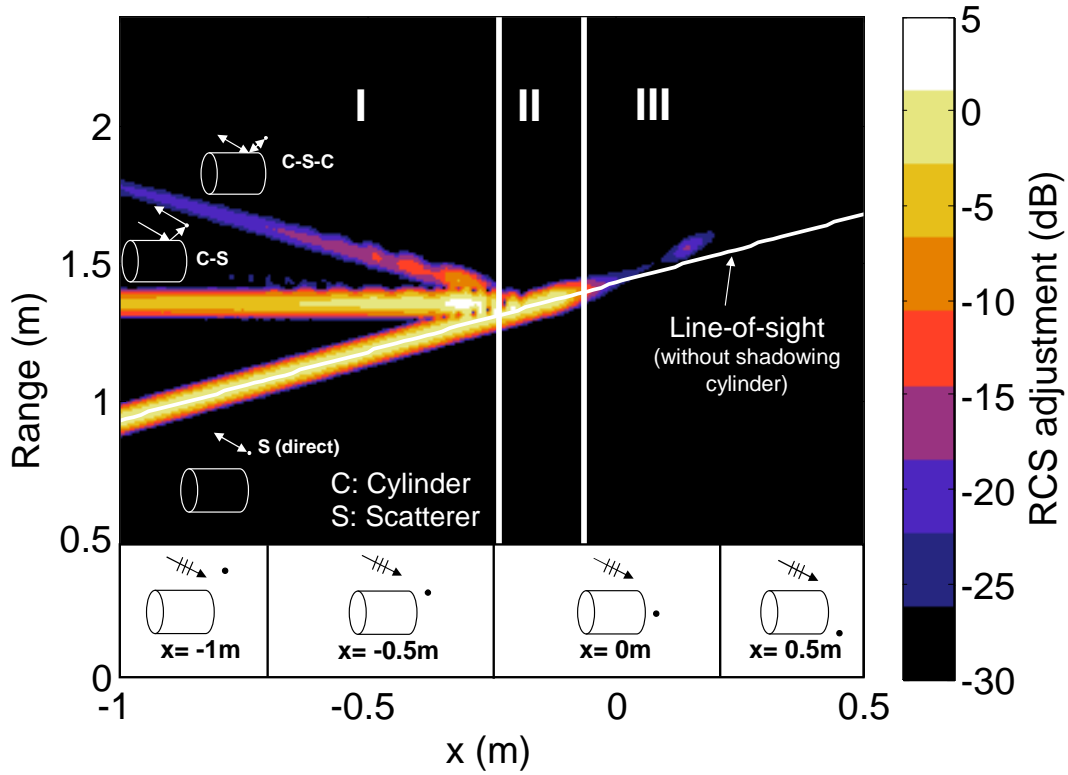


Fig. 8. Range-Time-Intensity (RTI) plot of predicted two-body correction factor (HH Polarization) showing multi-bounce returns.

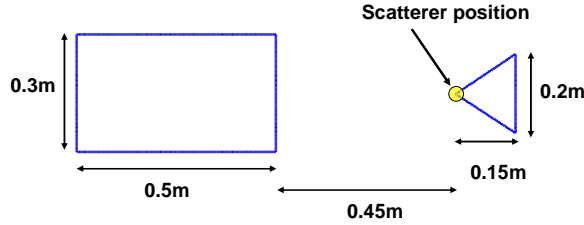


Fig. 9. Geometry of the cylinder-cone shadowing case, highlighting the scatterer of interest.

the scatterer is shadowed from both incident and reflected waves. It is only illuminated by energy diffracting off the edge of the cylinder. The variable path length introduced by diffraction also delays the scatterer return so that it appears to bend outrange before it is fully shadowed.

B. Cylinder-Cone Validation Case

Consider the geometry of Fig. 9. We consider the cylinder as the shadowing body and the cone as the shadowed body. In particular, we shall be concerned with the shadowing of the scatterer corresponding to the nose tip. Using the same field expressions for the finite cylinder as were used in Section III-A (found in the Appendix), we can compute the shadowing correction at the location of the nose tip. The scatterer RCS from the CICERO prediction for the cone was adjusted as described in this paper, and the results were compared to the CICERO prediction of the cylinder-cone complex. The same frequency band and imaging techniques were used here as in the two cylinder case.

The results for both linear polarizations are found in Fig. 10. The present model accurately predicts the scattering behavior for aspects near the shadow boundary. However, the CICERO shows a higher scatterer RCS near 180 degrees aspect, where perfect shadowing would be expected. Upon further examination, it was discovered that this was due to the specular return from the cylinder spilling over into the area occupied by the cone scatterer of interest, and does not represent an actual increase in the RCS of this scatterer.

C. Two Spheres Validation Case

The theoretical formulation of the shadowing model makes use of the exact expressions for the scattered near fields of a perfectly conducting sphere, which are well known [5]. To get an idea of the shadowing corrections, one can plot the square of the y -component of the magnetic field assuming the incident field is also y directed. This is proportional to g_{yy}^2 , which determines the shadowing correction. This quantity, normalized to the intensity of the incident plane wave, is plotted over a “screen” placed 2.54 cm (1”) behind a 49.53 cm (19.5”) sphere in Fig. 11. The frequency used for the shadowing computation is 10 GHz. One can see shadowing toward the center as expected, and also a bright spot at the center of the plane, due to constructive interference of the diffracted rays. Also notable are the ripples seen around the shadow boundary, also due to diffraction.

In this example case, a 30.48 cm (12”) diameter metal sphere is placed 2.54 cm behind a 49.53 cm diameter metal sphere, so that the geometry at 0 degrees aspect is shown in Fig. 12. The full near fields of the

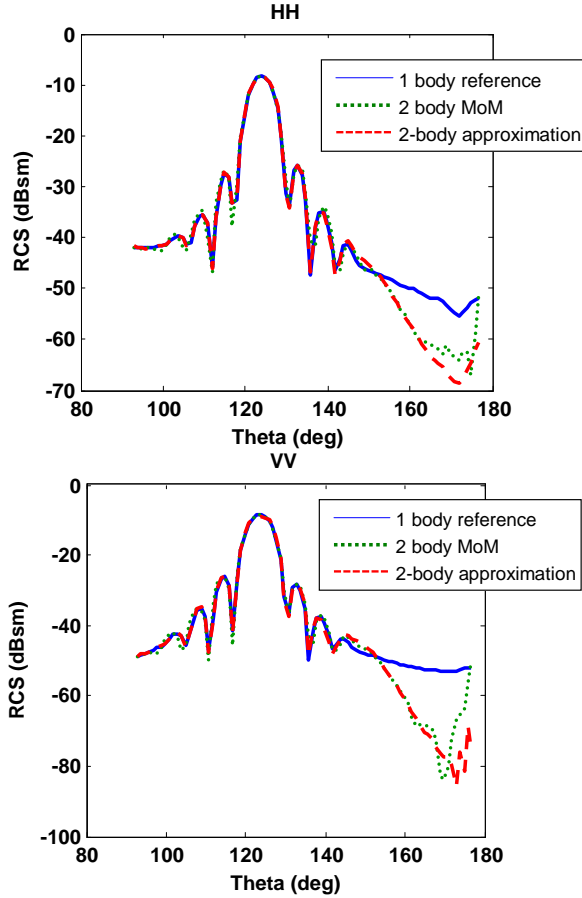


Fig. 10. Comparison of shadowing predictions for the cylinder-cone validation case for HH and VV polarization.

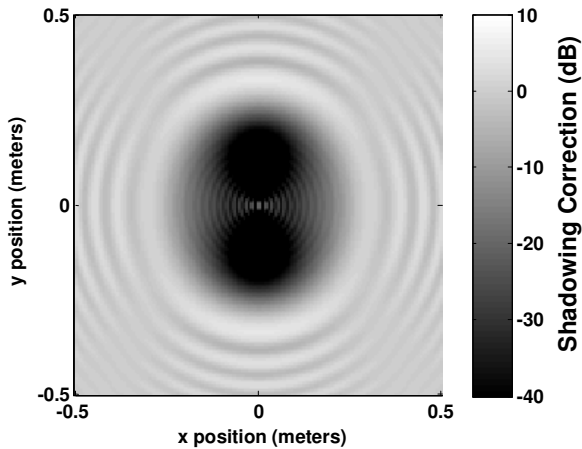


Fig. 11. Predicted shadowing correction (g_{yy}^2) for a 49.53 cm diameter sphere on a plane 2.54 cm behind the sphere. The incident magnetic field is along the y direction and propagates in the z direction.

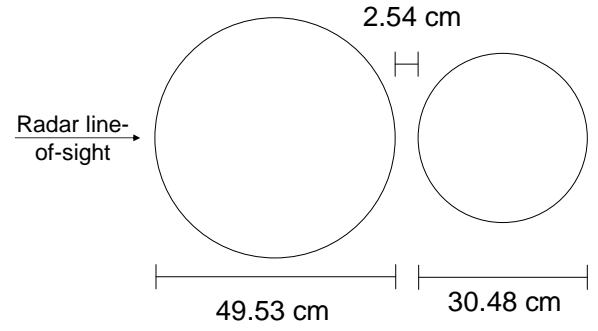


Fig. 12. Geometry of two spheres test case at 0 degrees aspect angle.

49.53 cm sphere are used by the present technique to adjust the scatterer intensity from the smaller sphere. X-band measurements of this target complex were carried out in the static range. Data were collected and compared to theory from 9-11 GHz at both VV and HH polarizations.

The spheres were placed with their centers aligned and rotated horizontally on a turntable in a static range. This allowed the response across various aspects to be measured. The magnitude of the point scatterer corresponding to the leading edge of the 30.48 cm sphere is extracted from the measured data using wideband imaging techniques. To perform the extraction, wideband images similar to Fig. 3 were used with a 5° integration window. The scatterer corresponding to the creeping wave is not considered. The results are shown in Fig. 13. Both the measurements and the theoretical predictions are plotted, as well as the MoM prediction.

For higher aspect angles where the 30.48 cm sphere begins to move in front of the 49.53 cm sphere, the point scatterer approximation assumed in the model of the 30.48 cm sphere breaks down, since the double bounce return causing the more pronounced lobes in the theoretical curve is in reality shielded by the 30.48 cm sphere. Overall, however, the accuracy of the current point scatterer shadowing model is reasonably close to the accuracy of the full wave solver in its prediction of the shadow boundary, while its implementation is much simpler. There appeared to be a small angular misalignment (roughly 1.5 degrees) of the measurement turntable, which was corrected in Fig. 13.

As was the case for the cylinder, the shadowing is greater at VV polarization than at HH. This can also be understood from the appearance of Fig. 11 in which the shadowing is much more pronounced along the y axis than along the x axis.

IV. CONCLUSION

A method has been presented to calculate the RCS of a two-body system where the scattered near fields of one of the two objects is known. This limits the validation cases to a set of problems where the shadowing object is a canonical shape (e.g., a conducting plate of arbitrary dimensions, cylinder, sphere, etc.). Given a point scatterer model of the other object (on which no shape restrictions are placed), the fields at these scattering centers together with reciprocity are used to calculate the adjusted RCS in the presence of the shadowing

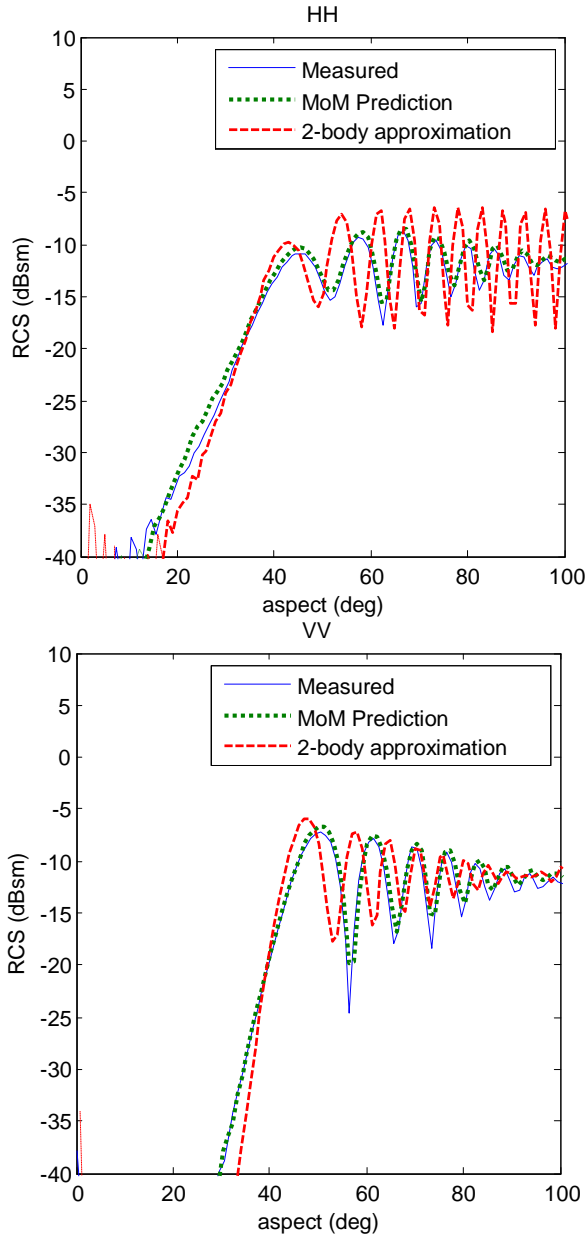


Fig. 13. Comparison of shadowing predictions for the two spheres validation case for VV and HH polarization. At zero degrees aspect, the sphere is shadowed by the 49.53 cm sphere.

body. Although any technique using only information from scattering center models (without full surface representation) is approximate, this method offers reasonably accurate scattering center adjustments which can be computed very rapidly without the need for a full-wave solver.

To validate our methodology, a MoM solver was used to predict scatterer RCS for a two-cylinder system and a cylinder-cone system, and static range measurements were compared to theory for the case of two conducting spheres. Good agreement was obtained between the shadowing characteristics predicted by the two-body model and both measurement and Moment Method simulation.

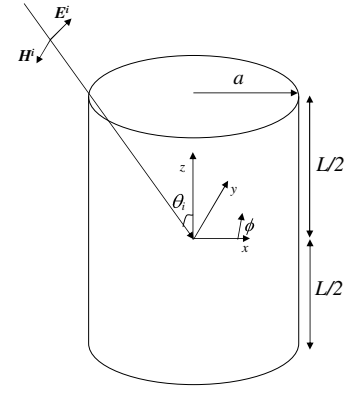


Fig. 14. Geometry for TM^z plane wave incident on conducting cylinder of finite length.

APPENDIX NEAR FIELDS OF A CONDUCTING CYLINDER

In this section, we calculate the approximate fields due to a finite, perfectly conducting cylinder, which were used in the calculations of Section III-A.

A. TM Case

Consider the cylinder of Fig. 14 with some finite length L . We begin by calculating the surface currents on the finite cylinder, assuming they are the same as they would be on a cylinder of infinite extent (thus neglecting endcaps and edge currents). Assuming TM^z incident polarization with

$$\mathbf{E}^i = E_0 (\hat{x} \cos \theta_i + \hat{z} \sin \theta_i) e^{-j\beta x \sin \theta_i} e^{j\beta z \cos \theta_i}, \quad (33)$$

we know from [6]

$$\begin{aligned} H_\phi^s &= -jE_0 \frac{1}{\eta} e^{j\beta z \cos \theta_i} \times \\ &\sum_{n=-\infty}^{\infty} j^{-n} a_n H_n^{(2)'}(\beta \rho \sin \theta_i) e^{jn\phi}, \\ H_z^s &= 0, \end{aligned}$$

where

$$a_n = \frac{-J_n(\beta a \sin \theta_i)}{H_n^{(2)}(\beta a \sin \theta_i)}. \quad (34)$$

Since the z -component of the scattered magnetic field is zero, and the ρ component is normal to the surface of the cylinder, only the ϕ component contributes to the surface current density J_z given by

$$\mathbf{J}_s = \hat{n} \times \mathbf{H} = \hat{\rho} \times H_\phi \hat{\phi} = H_\phi \hat{z}. \quad (35)$$

We can then calculate the surface current and integrate to find the fields everywhere. This yields

$$\begin{aligned}
H_\rho^s &= \frac{a^2}{4\pi} \int_0^{2\pi} d\phi' J_z^*(\phi') \sin(\phi - \phi') \times \\
&\quad \int_{-\frac{L}{2}}^{\frac{L}{2}} dz' \frac{-e^{-j\beta r} (j\beta r + 1)}{r^3} e^{j\beta z' \cos(\theta_i)} \\
H_\phi^s &= \frac{-a}{4\pi} \int_0^{2\pi} d\phi' J_z^*(\phi') (\rho - a \cos(\phi - \phi')) \times \\
&\quad \int_{-\frac{L}{2}}^{\frac{L}{2}} dz' \frac{-e^{-j\beta r} (j\beta r + 1)}{r^3} e^{j\beta z' \cos(\theta_i)},
\end{aligned} \quad (36)$$

where

$$J_z^*(\phi') = \frac{E_0}{\eta} [-\cos \phi' e^{-j\beta a \cos \phi' \sin \theta_i} + \quad (37)$$

$$\begin{aligned}
&j \sum_{n=0}^{\infty} \epsilon_n j^{-n} \frac{H_n^{(2)'}(\beta a \sin \theta_i)}{H_n^{(2)}(\beta a \sin \theta_i)} J_n(\beta a \sin \theta_i) \cos(n\phi'), \\
\epsilon_n &= \begin{cases} 2 & : n = 0 \\ 1 & : n \neq 0, \end{cases} \quad (38)
\end{aligned}$$

and

$$r = \sqrt{a^2 + \rho^2 - 2a\rho \cos(\phi - \phi') + (z - z')^2}. \quad (39)$$

The evaluation of (36) can now be carried out numerically.

B. TE Case

The derivation of the TE^z incidence case follows parallel to that of the TM case. We will see that the induced surface current density will have both z and ϕ components. This produces, in general, fields with ρ , ϕ , and z components.

We consider an obliquely-incident plane wave with an incident magnetic field is given by

$$\mathbf{H}^i = H_0(\hat{x} \cos \theta_i + \hat{z} \sin \theta_i) e^{-j\beta x \sin \theta_i} e^{j\beta z \cos \theta_i}. \quad (40)$$

Following [6], the scattered fields in cylindrical coordinates are given by

$$H_\rho^s = jH_0 \cos \theta_i e^{j\beta z \cos \theta_i} \sum_{n=-\infty}^{\infty} (-j)^n b_n H_n^{(2)'}(\beta \rho \sin \theta_i) e^{jn\phi} \quad (41)$$

$$H_\phi^s = jH_0 \frac{\cot \theta_i}{\beta \rho} e^{j\beta z \cos \theta_i} \sum_{n=-\infty}^{\infty} n(-j)^{n-1} b_n H_n^{(2)}(\beta \rho \sin \theta_i) e^{jn\phi} \quad (42)$$

$$H_z^s = H_0 \sin \theta_i e^{j\beta z \cos \theta_i} \sum_{n=-\infty}^{\infty} (-j)^n b_n H_n^{(2)}(\beta \rho \sin \theta_i) e^{jn\phi} \quad (43)$$

where

$$b_n = -\frac{J_n'(\beta a \sin \theta_i)}{H_n^{(2)'}(\beta a \sin \theta_i)}. \quad (44)$$

Differentiation, denoted by the prime, is with respect to the function's complete argument. We introduce the quantities

$$S_1(\phi) = \sum_{n=-\infty}^{\infty} (-j)^{n+1} \frac{e^{jn\phi}}{H_n^{(2)'}(\beta a \sin \theta_i)} \quad (45)$$

and

$$\begin{aligned}
S_2(\phi) &= \sum_{n=-\infty}^{\infty} (-j)^n [\sin \phi J_n(\beta a \sin \theta_i) \\
&\quad - \frac{n}{\beta a \sin \theta_i} \frac{J_n'(\beta a \sin \theta_i)}{H_n^{(2)'}(\beta a \sin \theta_i)} H_n^{(2)}(\beta a \sin \theta_i)] e^{jn\phi}.
\end{aligned} \quad (46)$$

The final expressions for the fields are

$$\begin{aligned}
H_\rho^s &= H_{\rho_1} + H_{\rho_2} \\
H_\phi^s &= H_{\phi_1} + H_{\phi_2},
\end{aligned} \quad (47)$$

where

$$\begin{aligned}
H_{\rho_1} &= \frac{H_0 a^2}{4\pi} \cos \theta_i \int_0^{2\pi} d\phi' \sin(\phi - \phi') S_2(\phi') \times \\
&\quad \int_{-L/2}^{L/2} dz' \frac{1 + j\beta r}{r^3} e^{-j\beta(r-z' \cos \theta_i)} \\
H_{\rho_2} &= \frac{-H_0}{2\pi^2 \beta} \int_0^{2\pi} d\phi' \cos(\phi - \phi') S_1(\phi') \times \\
&\quad \int_{-L/2}^{L/2} dz' (z - z') \frac{1 + j\beta r}{r^3} e^{-j\beta(r-z' \cos \theta_i)} \\
H_{\phi_1} &= \frac{H_0 a}{4\pi} \cos \theta_i \int_0^{2\pi} d\phi' [a \cos(\phi - \phi') - \rho] S_2(\phi') \times \\
&\quad \int_{-L/2}^{L/2} dz' \frac{1 + j\beta r}{r^3} e^{-j\beta(r-z' \cos \theta_i)} \\
H_{\phi_2} &= \frac{H_0}{2\pi^2 \beta} \int_0^{2\pi} d\phi' \sin(\phi - \phi') S_1(\phi') \times \\
&\quad \int_{-L/2}^{L/2} dz' (z - z') \frac{1 + j\beta r}{r^3} e^{-j\beta(r-z' \cos \theta_i)}
\end{aligned} \quad (48)$$

Also,

$$\begin{aligned}
H_z &= \frac{-H_0}{2\pi \beta} \int_0^{2\pi} d\phi' [a - \rho \cos(\phi - \phi')] S_1(\phi') \times \\
&\quad \int_{-L/2}^{L/2} dz' (z - z') \frac{1 + j\beta r}{r^3} e^{-j\beta(r-z' \cos \theta_i)}.
\end{aligned} \quad (49)$$

ACKNOWLEDGMENT

This research was sponsored by the U.S. Navy under Air Force contract FA8721-05-C-0002. Opinions, interpretations, conclusions and recommendations are those of the authors and are not necessarily endorsed by the U.S. Government.

REFERENCES

- [1] K. Sarabandi, P. Polatin, "Electromagnetic Scattering from Two Adjacent Objects," *IEEE Trans. Ant. Prop.*, vol. 42, no. 4, pp. 510-517, Apr. 1994.
- [2] Shu-Qing Li, Jing Fang, and Wen-Bing Wang, "Electromagnetic Scattering from Two Adjacent Cylinders," *IEEE Trans. Geoscience Remote Sensing*, vol. 36, no. 6, pp. 1981-1985, Nov. 1998.
- [3] G. Heath, "Properties of the linear polarization bistatic scattering matrix," *IEEE Trans. Ant. Prop.*, vol. 29, no. 3, pp. 523-525, May 1981.
- [4] L. N. Medgyesi-Mitschang, P. L. Huddleston, J. M. Putnam, "Radar Scattering Analysis: Computer Implementation and Code Listings, Volume II," McDonnell Douglas Research Laboratories Final Report, 22 November 1984.
- [5] J. A. Stratton, *Electromagnetic Theory*. New York: McGraw-Hill, 1941.
- [6] C. A. Balanis, *Advanced Engineering Electromagnetics*. New York: John Wiley & Sons, 1989.



Joshua L. Wilson was born in Milwaukee, WI in 1983. He received the Ph.D. degree in electrical engineering at the University of Tennessee, Knoxville in 2008.

He is currently a Technical Staff member at MIT Lincoln Laboratory in Lexington, MA, where his research activities include measurement and modeling of electromagnetic scattering and radar. Previously, he was a Research Assistant at Oak Ridge National Laboratory in Oak Ridge, TN where he conducted research on charged particle accelerator systems at

the Spallation Neutron Source.

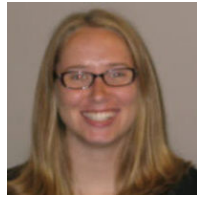


Brian W. Rybicki (S'06-M'09) was born in Salt Lake City, Utah in 1984. He received the B.S. (Honors) and M.S. degrees in electrical engineering from The Pennsylvania State University (Penn State), University Park, in 2006 and 2008, respectively.

He is currently an Associate Staff member at the Massachusetts Institute of Technology, Lincoln Laboratory (MIT LL), Lexington, working on radar signature generation and sensor analysis. Previously, he was a Research Assistant with the Computational

Electromagnetics and Antenna Research Laboratory (CEARL) at Penn State working on nanoantenna characterization and frequency selective surface design. His research interests include antenna design, radar cross section measurement, computational electromagnetics, and radar imaging.

Mr. Rybicki is a member of the IEEE Antennas and Propagation Society, Eta Kappa Nu and Tau Beta Pi.



Lea E. Johnson was born in Burnsville, Minnesota in 1986. She received a B.S. degree in electrical engineering from Michigan Technological University, Houghton in 2009.

She is currently an Assistant Staff member at the Massachusetts Institute of Technology, Lincoln Laboratory (MIT LL), Lexington, working on radar signature generation and sensor test planning. Previously, she was a summer intern for Rockwell Collins Inc. in Cedar Rapids, IA working on image change detection algorithms and image processing for a

persistent surveillance platform. Her research interests include radar cross section modeling, radar imaging and image processing.

Ms. Johnson is a member of the Society of Women Engineers.



Douglas M. Koltenuk was born in Delaware in 1972. He graduated from Yale University in 1993 with a B.S. degree in physics. In 1999, he received his Ph.D. in physics from the University of Pennsylvania. His thesis research on the electroproduction of kaons on hydrogen and deuterium was conducted at the Thomas Jefferson National Accelerator Facility in Newport News, VA.

In 1999 he joined MIT Lincoln Laboratory in Lexington, Massachusetts as a Technical Staff member. His research has included work on sidelobe

cancellers, air vehicle survivability, and helicopter-mounted UHF arrays. The majority of his research has focused on RF modeling and measurement of targets of interest to the ballistic missile defense community.